Wind and wave-induced currents over sloping bottom topography, with application to the Caspian Sea

Thesis for the degree of Philosophiae Doctor

Peygham Ghaffari
Faculty of Mathematics and Natural Sciences
University of Oslo
Norway

March 11, 2014

Series of dissertations submitted to the
Faculty of Mathematics and Natural Sciences, University of Oslo
No. 1470

ISSN 1501-7710

Cover: Inger Sandved Anfinsen.
Printed in Norway: AIT Oslo AS.

Produced in co-operation with Akademika Publishing.
The thesis is produced by Akademika Publishing merely in connection with the thesis defence. Kindly direct all inquiries regarding the thesis to the copyright holder or the unit which grants the doctorate.

Acknowledgement

Firstly, I am very grateful to my principal supervisor, Prof. Jan Erik H. Weber. Jan has always provided support, guidance and enthusiasm for this PhD. I appreciate his patience discussing, proof-reading and (most of all) for always looking for theoretical explanations. Thanks for being always helpful and supportive not only about scientific issues, but also with personal matters. Secondly, I would like to thank my second supervisor Prof. Joseph H. LaCasce, as well as Dr. Pål Erik Isachsen, for their valuable contributions. Many thanks to all friends and colleagues at the MetOs section for a great working environment. I wish to thank the Norwegian Quota Scheme for partial financial support during these years.

And last but not least, I would like to thank my family Mahnaz and Marina for their patience and being always supportive.

January, 2014

List of publications

The present thesis is entitled "Wind and wave-induced currents over sloping bottom topography, with application to the Caspian Sea", and is based on the following papers:

I- Ghaffari, P., Isachsen, P. E., and LaCasce, J. H.: 2013, Topographic effects on current variability in the Caspian Sea, *J. Geophys. Res.,* 118, pp 1-10.

II- Weber, J. E. H. and Ghaffari, P.: 2009, Mass transport in the Stokes edge wave, *J. Mar. Res.,* 67, 213-224.

II- Ghaffari, P. and Weber, J. E. H.: 2014, Mass transport in the Stokes edge wave for constant arbitrary bottom slope in a rotating ocean, *J. Phys. Oceanogr.,* doi:10.1175/JPO-D-13-0171.1, in press.

IV- Weber, J. E. H. and Ghaffari, P.: 2014, Mass transport in internal coastal Kelvin waves, *Europ. J. Mech. B/Fluids*, in press.

Contents

1 Introduction **1**

1.1 Thesis objectives 1

2 Theory **3**

2.1 On current variability over closed PV contours 3

2.1.1 Barotropic model 3

2.1.2 Equivalent Barotropic model 5

2.2 Wave-induced flow 7

2.3 On the Stokes edge wave 8

2.3.1 Mass transport in the Stokes edge wave in a rotating ocean 9

2.3.2 Mass transport in the Stokes edge wave in a non-rotating ocean 12

2.4 On internal waves 13

2.4.1 Mass transport in internal coastal Kelvin waves 14

3 Observations **16**

3.1 The Caspian Sea 16

3.2 Field measurements 18

3.2.1 Study area 18

3.2.2 Satellite observations 18

3.2.3 Current meter observations 18

3.2.4 Hydrographic observations 19

4 Results **22**

4.1 Topographic Effects on the Large-scale Flow Field in the Caspian Sea 22

4.2 Mass transport in the Stokes edge wave for constant arbitrary bottom slope . . . 26

4.3 Mass transport in internal coastal Kelvin waves 28

5 Concluding remarks **31**

Bibliography **31**

Chapter 1

Introduction

In the ocean basins topography and coasts may act to trap mechanical energy. This energy may be in the form of wind-driven currents along bottom contours or gravity waves along coasts or sloping beaches. Since waves do posses mean momentum when averaged over the wave cycle, i.e. the Stokes drift (*Stokes*, 1847), they induce a net transport of water particles in the same way as the more traditional wind-driven currents. Since these currents are trapped in regions close to the coast, or over bottom slopes in the coastal region, they may directly affect human activity and the coastal population through their ability to transport biological material, pollutants and sediments in suspension along the shore.

1.1 Thesis objectives

The first objective of the work presented in this thesis is to provide better understanding of the topographic effect on current variability. This is done by exploring specific topics where the effect of topography may alter the currents. In wind-induced current case, the dynamics of flows with closed potential vorticity (PV) contours is examined. Topography generally distorts the geostrophic currents. If the topography is steep enough, it dominates the stationary part of the potential vorticity, even causing closed PV contours. Therefore, mean flow can be excited and exist on the closed contours (without encountering with boundaries) by wind-forcing. At ocean depths that are intersected by topography, currents steer around major topographic features. In addition, particularly at high latitudes, where the ocean is weakly stratified (*Isachsen et al.*, 2003), geophysical flows tend to be vertically coherent (or barotropic) due to the rotation of the Earth. As a result currents near the ocean surface align in roughly the same direction as deep ocean currents, and consequently often follow contours of constant depth, e.g. see (*Gille et al.*, 2004). Most major currents respond to sea floor topography. In the present study, we investigated to what degree this mechanism works for the Caspian Sea which is a low latitude water body.

The second objective is to estimate the mean currents induced by trapped gravity waves. For that purpose, we investigated the Lagrangian mass transport in two different types of the gravity waves; the Stokes edge waves over sloping topography in a non-rotating and rotating ocean, and the internal coastal Kelvin wave. In practice, these waves are trapped due to a sloping bottom and the earth's rotation. In particular, the Lagrangian mass transport is obtained from the ver-

tically integrated equation of momentum and mass, correct to second order in wave steepness. The Lagrangian current is composed of a non-linear Stokes drift (inherent in the waves) and a mean vertically-averaged Eulerian current. When waves propagate along topography (along the coast), the effect of viscosity leads to a wave attenuation, and hence a radiation stress component. The Eulerian current arises as a balance between the radiation stress, bottom friction, and the Coriolis force in a rotating ocean. The associated Stokes drift and Eulerian currents are investigated for the aforementioned waves. Additionally, their contributions to the mean Lagrangian drift are examined. We wish to explore how the contributions of the Stokes drift and Eulerian current varies with factors such as slope angle, wave amplitude, wave length and the earth's rotation.

In order to address these objectives four papers are included in this thesis. Objective number 1 is treated in paper I (*Ghaffari et al.*, 2013), objective number 2 in papers II (*Weber and Ghaffari*, 2009), III (*Ghaffari and Weber*, 2014), and IV (*Weber and Ghaffari*, 2014).

The remaining part of this thesis is organized as follows: chapter 2 presents a brief theory, and chapter 3 provides a description of the study area. Results are presented and discussed in chapter 4. This is then followed by prints of the papers.

Chapter 2

Theory

This section provides a short theoretical background of the wind-induced current variability on closed PV contours. Additionally, some theory and explanation of the concept of wave-induced currents, i.e. Stokes drift and Eulerian current are given. The section also presents a brief overview of the Stokes edge wave, the internal coastal Kelvin wave, and the associated wave-induced drifts.

2.1 On current variability over closed PV contours

2.1.1 Barotropic model

Most major currents respond to sea floor topography. For instance, topography seems to steer the Antarctic Circumpolar Current (ACC) on certain part of its path (*Gordon et al.*, 1978). Also Gulf Stream and the Kuroshio Extension all steer around ridges and seamounts. It is the conservation of potential vorticity which confines a water parcel to the PV contours. Hence, the conservation equation for PV provides an equally powerful and simple tool for discussion of the mean oceanic circulation on climatic scales (time scale of several months, length scale of about 500 km (*Hasselmann*, 1982)). In fact, strong topography may dominate the stationary part of the PV, even causing closed PV contours. The dynamics of the closed PV contours is different from those with blocked contours. With closed contours it is possible to obtain steady flows parallel to the PV contours. Such mean flow, which is not present with blocked contours, can be excited by wind forcing (*Hasselmann*, 1982; *Kamenkovich*, 1962; *Greenspan*, 1990). The mass transport, the depth integrated horizontal velocity, can be modeled using an integral equation derived from shallow water equation. In the linear limit, the model assumes a balance between divergence in the surface Ekman layer and convergence in the bottom Ekman layer; the latter is achieved via a flow parallel to the PV contours (Fig. 2.1). The flow strength can be predicted, if one knows the wind stress and topography.

The theory is described by *Isachsen et al.* (2003). Consider a homogeneous ocean with a rigid lid and varying topography. Ignoring non-linearity and exploiting the Boussinesq approximation, the depth-integrated, horizontal momentum equation takes the form

$$\frac{\partial \vec{u}}{\partial t} + fk \times \vec{u} = -g\nabla\eta + \frac{1}{H}\left(\frac{\vec{\tau}_s}{\rho_0} - \vec{\tau}_b\right), \tag{2.1}$$

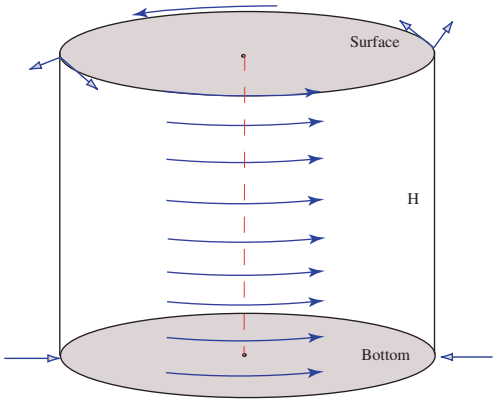

Figure 2.1: Schematic of barotropic model spin-up.

where u is horizontal velocity vector, f is the Coriolis parameter, η is the sea surface displacement, τ_s is the wind stress and τ_b is the bottom stress. Note that horizontal (eddy) diffusion of momentum is excluded. Taking the curl yields

$$\frac{\partial}{\partial t}\nabla \times \vec{u} + J(\psi, \frac{f}{H}) = k \cdot \nabla \times \left(\frac{\vec{\tau}_s}{\rho_0 H} - \frac{\vec{\tau}_b}{H} \right), \tag{2.2}$$

where J is the Jacobian operator and ψ is the transport stream function

$$\int_{-H}^{0} (u, v)\, dz = (-\psi_x, \psi_y)\,. \tag{2.3}$$

The dominant term in (2.2) is the second one and that the temporal variability, wind forcing and bottom drag are comparably small. This implies that the first-order flow is parallel to the f/H contours. Therefore, to the extent that oceanographic flows are barotropic, they should be steered along f/H contours. Assuming a linear bottom drag in line with Ekman damping, so that $\tau_b = R\vec{u}$ (R is the bottom friction coefficient), and integrating (2.2) over an area bounded by an f/H contour yields

$$\frac{\partial}{\partial t} \oint_{f/H} \vec{u} \cdot dl = \frac{1}{\rho_0 H} \oint_{f/H} \tau_s \cdot dl - \frac{R}{H} \oint_{f/H} \vec{u} \cdot dl, \tag{2.4}$$

after applying Stokes' theorem. The fist term on the right hand side is the net Ekman transport in or out of the surface layer and the last term is the net transport in the bottom layer. An imbalance between them determines a circulation pattern around the closed contour. In order to get better impression about the response of the flow to forcing, it is convenient to take a Fourier transform in time, which gives

$$\vec{U}_0 = \left(\frac{k}{H} \times \nabla \frac{f}{H} \right) \mathrm{Re} \left[\frac{\oint_{f/H} \rho_0^{-1} H^{-1} \vec{\tau}_s \cdot dl}{\oint_{f/H} H^{-1} (r + i\omega) \left(\nabla \frac{f}{H} \cdot \vec{n} \right) dl} \right], \tag{2.5}$$

where $r = R/H$ is an inverse frictional damping time scale and n is the surface normal unit vector. Therefore, the surface circulation depends on the bottom friction and the forcing frequency. Additionally, the model can be used to study Sea Surface Hight (SSH) variabilities by determining the difference in Sea Level Anomalies (SLA) between different f/H contours

$$\frac{\partial \eta_0}{\partial (f/H)} = \left(\frac{f}{g}\right) \mathrm{Re}\left[\frac{\oint_{f/H} \rho_0^{-1} H^{-1} \vec{\tau}_s \cdot dl}{\oint_{f/H} H^{-1} (r + i\omega) \left(\nabla \frac{f}{H} \cdot \vec{n}\right) dl}\right]. \tag{2.6}$$

The velocities resulting from the barotropic model are parallel to the PV contours, and SSH displacements and the geostrophic velocities are inversely proportional to the bottom friction coefficient. For example, assume the wind stress has a single frequency, $\vec{\tau} = \vec{\tau}_0 \cos(\omega t)$. The velocity is then

$$\oint_{f/H} \vec{u} \cdot dl = \frac{\vec{\tau}_0}{r^2 + \omega^2} \left[r \cos(\omega t) + \omega \sin(\omega t)\right] \tag{2.7}$$

From this it is evident that

$$\oint_{f/H} \vec{u} \cdot dl \sim \frac{\vec{\tau}_0}{\omega} \sin(\omega t), \quad r \leq \omega, \qquad \oint_{f/H} \vec{u} \cdot dl \sim \frac{\vec{\tau}_0}{r} \cos(\omega t), \quad r \geq \omega.$$

At frequency much lower than r, the response is in phase with the wind and inversely proportional to r. At high frequencies, the amplitude is independent of r and the response lags the wind by $\pi/2$. Barotropic theory is often supported by observations. For example, floats in the Atlantic and Pacific Oceans preferentially spread along f/H contours rather than across them, indicating that flow responds to topography (LaCasce, 2000).

2.1.2 Equivalent Barotropic model

In practice, since the ocean is stratified, and velocities tend to be faster near the ocean surface than at mid-depth (Fig. 2.2), flow does not literally follow contours of f/H. *Gille et al.* (2004) used float data to examine whether Southern Ocean velocities could be assumed to be equivalent barotropic (EB), meaning that velocities attenuate with depth, with a fixed e-folding scale (*Killworth*, 1992). In such a flow field the mean velocity is close to self-similar in the vertical direction, i.e., velocity at one depth is parallel and also proportional to the velocity at adjacent depth (*Krupitsky et al.*, 1996). An EB model considers the velocity structure as EB. The conventional barotropic model is a particular case of the EB model. Such models widely known in atmospheric sciences since the application to the numerical weather forecasting by *Charney and Eliassen* (1949). Primarily similar approach was used to estimate the density distribution in the ocean. Later on, such models have been studied in the context of the Southern Ocean (*Ivchenko et al.*, 1999; *Krupitsky et al.*, 1996; *LaCasce and Isachsen*, 2010).

As it mentioned before, in an EB flow, the variables (e.g. velocity and pressure) vary with depth, but the direction of flow does not. Thus, horizontal velocity vector and pressure can be define in terms of surface velocity and pressure and a vertical structure function as

$$(p, \vec{u})(x, y, z, t) = (p_s, \vec{u}_s)(x, y, t) P(z), \tag{2.8}$$

where $\vec{u}$, $\vec{u}_s$ and p, p_s are velocity and pressure and their corresponding surface values, respec-

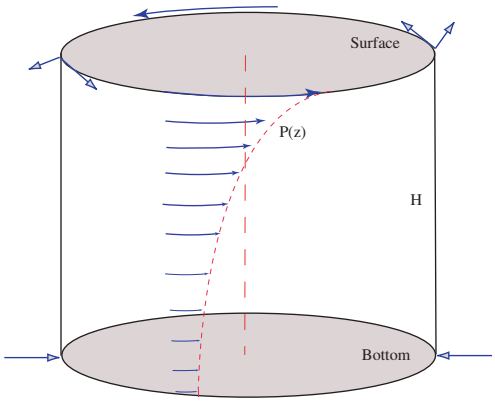

Figure 2.2: Schematic of equivalent barotropic model spin-up.

tively. $P(z) = \exp(z/h_0)$ is a vertical structure function, where h_0 is e-folding scale.

Assuming a linear bottom drag in line with *Isachsen et al.* (2003), yields $\vec{\tau}_b = R\vec{u}(-H) = r_e\vec{u}_s$, where R is the bottom friction coefficient, and r_e is modified drag coefficient. Noting that the surface pressure is proportional to the sea surface height, η, and substituting these into linear depth-integrated horizontal momentum equation and taking curl yields the equivalent barotropic potential vorticity equation

$$\frac{\partial}{\partial t}\nabla \times \vec{u}_s + J\left(\psi, \frac{f}{F}\right) = \nabla \times \frac{\vec{\tau}_s}{\rho_0 F} - \nabla \times \frac{r_e\vec{u}_s}{F}, \tag{2.9}$$

where ψ is transport streamfunction and Jacobian term $J(\psi, f/F) = F\vec{u}_s \cdot \nabla(f/F)$ is the advection of PV by flow. Under this assumption, (2.9) is dominated by the advection term, i.e. $J(\psi, f/F) = 0$. Therefore, flow is predicted to follow contours of f/F, i.e. the geostrophic contours in the EB model, where $F = h_0\left[1 - exp(-H/h_0)\right]$ (e.g. (*Marshall*, 1995; *Krupitsky et al.*, 1996; *LaCasce and Isachsen*, 2010)). Baroclinicity of the velocity structure determines e-folding scale. For small e-folding scales, i.e. for $h_0 \leq H$, F is approximately constant and the PV gradient is dominated by planetary β. In the limit where the e-folding scale, h_0, is infinite, this is equivalent to assuming that flow follows f/H contours, and the barotropic model is recovered.

The flow response to forcing can be better understood by invoking the continuity equation and eliminating the advection term by integrating (2.9) over a closed f/F contour.Taking a Fourier transform in time yields

$$\oint_{f/F}\left(i\omega + \frac{r_e}{F}\right)\vec{\tilde{u}}_s \cdot dl = \oint_{f/F}\frac{\vec{\tilde{\tau}}_s}{\rho_0 F} \cdot dl, \tag{2.10}$$

where $\left[\vec{\tau}_s,\ \vec{u}_s\right](x, y, t) = \sum_\omega \left[\vec{\tilde{\tau}}_s,\ \vec{\tilde{u}}_s\right](x, y, \omega)\exp(i\omega t)$. An inbalance between the net diverging or converging Ekman transport, i.e. RHS term in (2.10), and the net transport in the bottom layer, i.e. the second term on the LHS in (2.10), results in a change in the circulation around closed PV contour. Here the surface circulation depends on the modified bottom friction co-

efficient, the forcing frequency, and modified depth, F. At low frequencies ($\omega \ll r_e/F$), the circulation is in phase with the forcing. At very high frequencies, the circulation lags the wind by $\pi/2$, and is independent of the friction. The EB model flow senses less topographic control than a barotropic one. The lowest-order velocity at everywhere on the closed PV contour and SLA can be determined from (2.10).

2.2 Wave-induced flow

A net particle drift may occur for all cases of progressive wave motion (e.g. water waves, tides and atmospheric waves). *Stokes* (1846) derived expressions for water wave drift in an inviscid fluid. This nonlinear phenomenon extended to viscous fluids by *Longuet-Higgins* (1953). When we consider linear waves, the particles move in closed circles in deep water. But, without linearization, the individual fluid particles have a net drift in the direction of wave propagation. In reality, the path of the fluid particles under progressive waves has a nearly closed shape. But, the velocity of the fluid particles is slightly larger near the surface, than deeper down. Hence, averaging the particles trajectory over a predefined amount of time, i.e. one wave period, yields a small displacement of the particle in the direction of the wave propagation, i.e. the Stokes drift (Fig. 2.3).

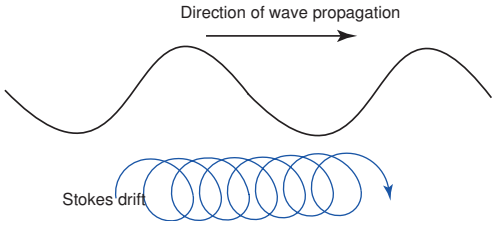

Figure 2.3: Sketch of nonlinear motion of a fluid particle due to propagating wave.

The Stokes drift is important for understanding the fundamentals in surface ocean dynamics and mixing. In particular, it plays an essential role in the oceanic Langmuir circulation (*McWilliams et al.*, 1997). Concerning its applications, adding an accurate assessment of the Stokes drift in ocean model systems is of utmost importance in mapping out surface dynamics, and increases the predictability of surface currents (*Röhrs et al.*, 2012). Furthermore, Stokes drift should be considered as an important factor in coastal process studies, especially in the area of sediment transport, see e.g. (*Longuet-Higgins*, 1953; *Nielsen*, 1992; *Vittori and Blondeaux*, 1996; *Blondeaux et al.*, 2002, 2012).

Consider a fluid particle initially located at $\vec{r}_o = (x_0, y_0, z_0)$ at time $t = t_0$, shifting to $\vec{r}_L = \vec{r}_0 + D\vec{r}$ at a later time t. The expression $D\vec{r} = \int_{t_0}^{t} \vec{v}_L(\vec{r}_0, t')dt'$ determines the fluid particle displacement in the time interval $t - t_0$, where $\vec{v}_L$ is Lagrangian velocity. The net displacement of the particles under wave influence can be obtained from the Lagrangian velocity. With regard to Eulerian specification, the relation between Lagrangian and Eulerian velocities is

$$\vec{v}_L(\vec{r}_0, t) = \vec{v}_E(\vec{r}_L, t) = \vec{v}_E(\vec{r}_0 + D\vec{r}, t). \tag{2.11}$$

Hence, from a Taylor series expansion we obtain

$$\vec{v}_L(\vec{r}_0, t) = \vec{v}_E(\vec{r}_0, t) + D\vec{r} \cdot \nabla_L \vec{v}_E + (\mathcal{H}.\mathcal{O}.). \tag{2.12}$$

The first term on the RHS is traditional Eulerian velocity, while the second term is the Stokes drift ($\vec{v}_S$). The ratio of the second term of (2.12) to the first term is of the order of the wave steepness ($\epsilon = kA$). Under the hypothesis of small wave steepness, the difference between $\vec{v}_L$ and $\vec{v}_E$ is negligible in the second term. Thus, the mean Lagrangian velocity correct to the second order wave steepness is given by

$$\bar{\vec{v}}_L = \bar{\vec{v}}_E + \bar{\vec{v}}_S, \tag{2.13}$$

where $D\vec{r} = \int_{t_0}^{t} \vec{v}_E(\vec{r}_0, t')dt'$, and the balance to the second order is obtained by averaging (2.12) over a wave period, denoted by an over-bar. Hence, the Lagrangian mean current is composed of Stokes drift plus a mean Eulerian current. While the former is inherent in the wave itself, the later depends on friction. Since the Stokes drift arises from the average of the wave motion along a Lagrangian trajectory, it is relevant for all floating and suspended particles present in the water column, and not only for fluid particles considered in the original derivation. This drift is basically related to the net particle motion in inviscid waves, and there is no Stokes drift in the cross-wave direction.

2.3 On the Stokes edge wave

Before we commence on this task, it would be appropriate to indicate why an understanding of this phenomenon, and the mechanisms that can bring it about, are important. Although, from Stokes' time to at least the later editions of Lamb's text on hydrodynamics it was generally thought that the edge waves were a mathematical curiosity, this is no longer the case. Apparently, many near-shore processes are controlled (or significantly affected) by the presence of edge waves (*LeBlond and Mysak*, 1978). Thus, edge waves play an important role in the dynamics of the coastal zone, beach erosion processes, and energy and momentum transfer (*Ghaffari and Weber*, 2014; *Weber and Ghaffari*, 2009; *Weber and Støylen*, 2011). Standing edge waves, in particular, is likely to have an observable effect on beach erosion and, perhaps, on the formation of sand bars close inshore. Edge waves are often considered as the major factor of the long-term evolution of the irregular coastal line, forming rhythmic crecentic bars (*Bowen and Inman*, 1971; *Kurkin and Pelinovsky*, 2003). These, and other more practical aspects, are described in *Howd et al.* (1992) and in the many papers cited therein. Our main concern in this study is the Stokes edge wave (*Stokes*, 1846) and the associated mass transport, which is the first mode in the spectrum of the shelf mode that contains both discrete and continuous parts, e.g. see (*Eckart*, 1951; *Ursell*, 1952; *Reid*, 1958). The essential features of this solution are described in *Lamb* (1932), although it was *Ursell* (1952) which gave the first complete description of the linear problem (being a mixture of continuous and discrete spectra). Several mechanisms for edge wave generation are possible in nature; Direct wind stress, passing atmospheric fronts, and tsunamis can generate large-scale; nonlinear interaction of wave groups and subharmonic resonance may trigger medium and small-scale edge waves, e.g. see (*Ghaffari and Weber*, 2014;

Weber and Ghaffari, 2009). Other mechanisms for the generation of edge waves are described by *Evans* (1989).

2.3.1 Mass transport in the Stokes edge wave in a rotating ocean

In earlier studies mass transport associated to edge waves has been investigated in the viscous laminar bottom boundary layer (*Dore*, 1975; *Mok and Yeh*, 1999). In practice, bottom boundary layers are turbulent and an additional mean interior Eulerian current is generated by frictional effect at the bottom. In this section we focus on the mass transport induced by the Stokes edge waves in a turbulent ocean.

We consider trapped surface gravity waves in a homogeneous rotating ocean ($f > 0$), with a linearly sloping bottom. The motion is described in Cartesian coordinate system, where x-axis is situated at undisturbed surface and directed into the semi-infinite ocean, y-axis is directed along coastline. The bottom is given by $z = -h = -x\tan\beta$, where $\beta\,(\leq \pi/2)$ is the slope angle, and free surface by $z = \eta$. Mean horizontal volume fluxes are defined as depth integrated

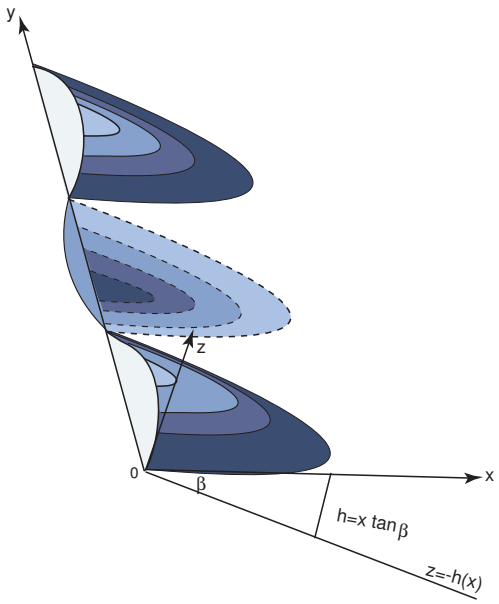

Figure 2.4: Sketch depicting the coordinate system, with the surface and sloping bottom included; y-axis is the along-shore coordinate and the seawards direction is $x \to \infty$.

velocities

$$\bar{U} = \overline{\int_{-h}^{\eta} u dz}, \qquad \bar{V} = \overline{\int_{-h}^{\eta} v dz}. \tag{2.14}$$

Since the velocities are integrated between material surfaces, they are actually the Lagrangian fluxes (*Phillips*, 1966; *Weber et al.*, 2006). Integrating the governing equations in the vertical between material surfaces, and utilizing full nonlinear boundary conditions, we obtain the mean

wave induced drift correct to second order in wave steepness (*Phillips*, 1966)

$$\frac{\partial \bar{U}}{\partial t} - f\bar{V} + gh\frac{\partial \bar{\eta}}{\partial x} = -\frac{\partial}{\partial x}\int_{-h}^{0}\frac{\bar{p}_d}{\rho}\,dz - \frac{g}{2}\frac{\partial}{\partial x}\overline{\tilde{\eta}^2} +$$

$$\frac{\bar{p}_d(-h)}{\rho}\tan\beta - \frac{\partial}{\partial x}\int_{-h}^{0}\overline{\tilde{u}\tilde{u}}\,dz - \frac{\partial}{\partial y}\int_{-h}^{0}\overline{\tilde{u}\tilde{v}}\,dz - \tau_1$$

$$\frac{\partial \bar{V}}{\partial t} + f\bar{U} + gh\frac{\partial \bar{\eta}}{\partial y} = -\frac{\partial}{\partial y}\int_{-h}^{0}\frac{\bar{p}_d}{\rho}\,dz \tag{2.15}$$

$$-\frac{g}{2}\frac{\partial}{\partial y}\overline{\tilde{\eta}^2} - \frac{\partial}{\partial x}\int_{-h}^{0}\overline{\tilde{u}\tilde{v}}\,dz - \frac{\partial}{\partial y}\int_{-h}^{0}\overline{\tilde{v}\tilde{v}}\,dz - \tau_2,$$

$$\frac{\partial \bar{\eta}}{\partial t} = -\frac{\partial \bar{U}}{\partial x} - \frac{\partial \bar{V}}{\partial y},$$

where, g is the gravitational acceleration, tilde represents wave quantities, and $\bar{p}_d$ is the non-hydrostatic (dynamic) pressure. Here, τ_1 and τ_2 are the mean turbulent bottom stress components per unit density in x and y-axis direction, respectively. The mean bottom pressure term in the x-momentum, i.e. $\bar{p}_d(-h)\tan\beta/\rho$, was missing from Phillips' derivation; see *Mei* (1973); *Ghaffari and Weber* (2014); *Weber and Ghaffari* (2009). Above equations set contains non-linear wave forcing terms. The wave-induced mass transport which is calculated indeed is Lagrangian transport; Stokes drift plus Eulerian mean current arise by friction. We separate the effect of friction on the wave motion and the mean flow. In this problem the oscillatory wave motion is influenced by viscosity acting in thin surface and bottom boundary layers. Within the top and bottom boundary layers the wave velocity varies rapidly with height, while in the interior part the variation is that of inviscid waves.

In this analysis we assume that the boundary layers thickness (δ) are quite thin, i.e. $\delta < h$, hence, its contribution in wave velocity is negligible. Therefore, for the linear wave we impose a no-slip, no surface stress condition and only the inviscid part of the solution with a damped amplitude is used. The damping rate is determined by bottom boundary layer in shallow-water with a no-slip bottom. While, in deep water the corresponding damping rate is proportional to the square of the wave number. Hence, for a given wavelength, the Stokes edge wave at certain distance from the coast may be characterized as a shallow-water or a deep-water wave for small and large slope angles, respectively. We have resorted an averaging procedure for determining the damping rate using the total mean energy and mean dissipation in the trapped zone, for all admissible slope angles.

The linearized equations for the damped interior wave motion by adopting the aforementioned approach become

$$\vec{\tilde{u}} = -f\hat{k}\times\vec{\tilde{u}} - \frac{1}{\rho}\nabla p - g\hat{k} - r\vec{\tilde{u}}, \qquad \nabla\cdot\vec{\tilde{u}} = 0, \tag{2.16}$$

where $\hat{k}$ is unit vector in z-direction. The resulting linearized surface wave, which is trapped

and may travel in both direction along the coast, is

$$\tilde{\eta} = \eta_0 \exp(q) \cos(\theta), \tag{2.17}$$

where η_0 is arbitrary constant, $q = -a_r x - \alpha y + b_r z$ is the exponential decay, and $\theta = -a_i x + k y + b_i z - \omega t$ is the phase function. Additionally, $a = a_r + i a_i$ and $b = b_r + i b_i$ are complex parameters. In that connection, it can be readily seen that trapping at the coast requires $a_r > 0$. In this calculation a_r has two roots, i.e. a_{r+} and a_{r-}. In order to have trapped wave propagating in positive and negative along-shore directions, we must exclude the a_{r-} solution. In this analysis we take that the frequency ω is real, while the wave number is complex, i.e. we consider spatial damping waves. Hence,

$$\kappa = k + i\alpha, \tag{2.18}$$

where α is the spatial damping rate in along-shore direction. The effect of the friction is attenuating the real part of the wave velocity components show that the wave motion in the Stokes edge wave occurs in planes parallel to the sloping bottom.

Following *Longuet-Higgins* (1953), the along-shore Stokes flux to the second order in wave steepness can be easily obtained from linear wave solution by integrating Stokes drift in vertical between material surfaces. However, in vertical limit ($\beta = \pi/2$) the problem should be treated with some care. In this case, trapping requires $\omega < 0$, and the resulting motion is coastal Kelvin wave propagating with the coast, i.e. the vertical wall, to the right ($f > 0$). In this limit the Stokes flux must be obtained by integrating the Stokes drift in vertical from minus infinity to zero. As discussed in section 2.2, the Stokes drift is related to the net particle motion in inviscid waves. Therefore, there is no Stokes drift in cross-wave direction. However, the presence of friction in the fluid introduce a small drift in the cross wave propagating direction, which is inseparable from Eulerian current. Hence, we take the Stokes flux in x-direction is zero, and only the along-shore Stokes flux contributes in total wave momentum (M_w), in the trapped zone. By comparing with total energy density in the trapped zone, we note that $E = M_w c^*$, where $c^* = \omega/k - (f \cos\beta)/(2k)$.

The mean wave-induced Lagrangian fluxes are obtained by integrating the momentum equation in vertical between material surfaces (2.15). The mean motion in cross-shore direction is quite small, and we neglect the effect of friction in this direction. But, the friction term in the along-shore direction must be modeled. It is almost common to use a bottom stress proportional to the square of the mean velocity (*Weber and Ghaffari*, 2009; *Weber and Støylen*, 2011). Defining and using a friction coefficient that is proportional to characteristic velocity; see *Nøst* (1994), not only provides identical effect, but also makes bottom friction linear in terms of the mean velocity. The present approach separates the decay of wave momentum from the frictional influence on the mean flow (*Jenkins*, 1989; *Weber and Melsom*, 1993; *Ardhuin and Jenkins*, 2006). As the cross-shore Stokes flux is zero in this problem, following *Phillips* (1966) the mean Eulerian volume flux in this problem can be written

$$\bar{U}_E = \bar{U}_L, \qquad \bar{V}_E = \bar{V}_L - \bar{V}_S, \tag{2.19}$$

where subscripts L, E, and S denote the Lagrangian, the Eulerian and the Stokes fluxes, re-

spectively. Utilizing 2.19, the steady state governing momentum equations 2.15 then reduce to

$$x\frac{\partial^2 \tau_2}{\partial x^2} - 2\alpha f \bar{V}_E = 2\alpha \left(f\bar{V}_S - \frac{\partial S}{\partial x} \right), \tag{2.20}$$

where S is the total wave-forcing stress component (*Ghaffari and Weber*, 2014). We introduce a non-dimensional Eulerian velocity Q_E and the non-dimensional Stokes drift velocity Q_S. Eventually, the vertically-averaged non-dimensional Lagrangian drift velocity Q_L becomes

$$Q_L = Q_E + Q_S \tag{2.21}$$

The non-dimensional form of 2.20 indicates that for the damped Stokes edge wave that propagate in with the coast to the left in the northern hemisphere, both induced Stokes drift and fractionally induced Eulerian current are trapped over the slope. On the other hand, for the damped Stokes edge wave propagating with the coast to the right, the induced Stokes drift is trapped over the slope, but the Eulerian current is not trapped. Solutions of the non-dimensional form of (2.20) attained using exponential integrals and numerical evaluation.

2.3.2 Mass transport in the Stokes edge wave in a non-rotating ocean

In this study we look at the Stokes edge waves in a non-rotating ocean. Therefore, the terms corresponded to the Coriolis force are disregarded from the momentum equation. We apply an analysis similar to that of rotating ocean. We consider trapped surface gravity waves in a homogeneous incompressible fluid with linearly sloping bottom. The motion is described in a Cartesian system, with similar configuration as section 2.3.1. We investigate the nonlinear mass transport by applying an Eulerian description of motion, and expanding the solution in series after wave steepness as small parameter. An analytical expression for the vertically-averaged Lagrangian drift velocity is derived by integrating the governing equations in the vertical between material surfaces. Utilizing the full nonlinear boundary conditions at the free surface and the sloping bottom, we obtain the mean quantities correct to second order in wave steepness. This drift is composed of Stokes drift plus Eulerian drift arises from the effect of friction. Here, the effect of friction on the wave motion and the mean flow should be separated. In general; for deep water waves, viscosity will affect the motion in the bulk of fluid, while for shallow water the viscous boundary layer at the bottom will dominate. In both cases the potential part of the wave field will attenuate exponentially in time. We can obtain the potential part of the wave field by using a friction that is linear in the wave velocity, e.i. $-r\vec{\tilde{u}}$, where constant friction coefficient r depends on viscosity. We can apply the potential theory of *Stokes* (1846), since this friction does not introduce vorticity into the fluid. Therefore, we can write the linearized complex velocity potential for the spatially damped Stokes edge wave in non-rotating ocean as

$$\tilde{\phi} = -\frac{i\eta_0\omega}{k\sin\beta} \exp\left(-kx\cos\beta - kz\sin\beta - \alpha y + i\left(ky - \alpha x\cos\beta + \alpha z\sin\beta - \omega t\right)\right), \tag{2.22}$$

where η_0 is wave amplitude, ω is wave frequency. Due to friction, the wave number κ in y-direction is complex, i.e. $\kappa = k + i\alpha$, where α is the small spatial attenuation coefficient. Introducing the velocity potential makes the problem quite easy to obtain analytical expressions.

Following *Longuet-Higgins* (1953), the Stokes drift to second order in wave steepness for this problem is easily obtained from the linear wave solution.

In order to evaluate the steady mass transport, the turbulent bottom stresses are modeled as to be proportional to the square of the mean Eulerian flux $\bar{V}_E$. The bottom friction is neglected in the direction normal to the wave propagating direction, as the velocities are small. Therefore, turbulent bottom stress in along-shore direction can be written as

$$\frac{\bar{\tau}}{\rho} = \frac{c_D|\bar{V}_E|\bar{V}_E}{h^2}, \tag{2.23}$$

where c_D is a bottom drag coefficient, ρ is density, and h is local depth. The friction induced along-shore mean Eulerian volume flux becomes

$$\bar{V}_E = \bar{V}_L - \bar{V}_S, \tag{2.24}$$

where the mean Lagrangian flux, $\bar{V}_L$, is derived by integrating the governing equations in the vertical between material surfaces, and the Stokes flux is readily obtained from linear wave field. Furthermore, it is easy to show that $|\bar{U}_E/\bar{V}_E| = \mathcal{O}(\alpha/k)$, which justifies the neglect of the cross-shore velocity in the bottom drag. We realize that this problem is the special case of the Stokes edge waves in the rotating ocean. By excluding the Coriolis parameter $(f = 0)$, from the expressions, all quantities in the rotating case simply recover the non-rotating case quantities; see *Ghaffari and Weber* (2014).

2.4 On internal waves

In general, gravity waves can form at the interface between fluids of different densities or in fluids with a continuous (stable) stratification. Most bodies of water at mid and lower latitudes have a pronounced vertical stratification. Internal waves can be triggered in a variety of ways, e.g. by the action of moving weather fronts, tides, wind stress, boats, currents moving over topography. Since the density difference between different layers in a stratified fluid is quite small, internal waves appear with longer periods, and larger amplitudes when compared to surface gravity waves. Internal waves are ubiquitous in the interior of the oceans and have been the focus of much attention in recent years due to their role in oceanic mixing and mass transport. Nonlinear effects associated with internal waves include the transport of water along with suspended mass such as sediment, nutrients, larvae, as well as contaminants. The details of such effects are crucial to the understanding of a wide array of physical situations where transport by internal waves is inherent. *Leichter et al.* (1996) showed that internal tides play an important role in relocating of larvae and other organisms to the near shore, and have remarkable influence in the development of the benthic communities. Additionally, they showed that the spatial distribution of plankton and consequently nutrient dispersal in coastal regions are strongly influenced by high frequency internal waves. Internal waves can be of particular interest in terms of the transport of contaminants at beaches (*Boehm et al.*, 2002a,b).

2.4.1 Mass transport in internal coastal Kelvin waves

In small bodies of water with negligible tidal forcing, internal waves appear to be triggered by temporal/spatial variation of the wind field. A stable stratified configuration along with a straight coastline, makes that coastal region to act as a waveguide for internal Kelvin waves. It is common to use a reduced-gravity model, which consider two layers of constant density, e.i. the upper thin and active, and the lower deep and quiescent layer, in such configurations. We will not use the reduce gravity model, as it filters out the higher baroclinic modes, and provides an erroneous results for the Stokes drift. The main focus of the present study is the main drift induced by internal coastal Kelvin waves. That drift may have influence on relocating bio-materials, suspended loads, pollutants, and also may be contribute in general circulations of the water bodies in question. We consider a stratified ocean of constant depth H, and Cartesian coordinate system, where the x-axis is directed in along-shore, and y-axis directed cross-shore. By using an Eulerian description of motion, and exploiting the hydrostatic approximation and

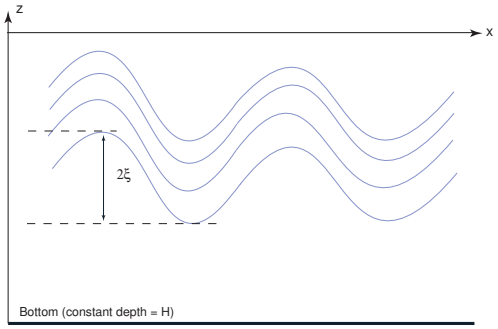

Figure 2.5: Sketch depicting the coordinate system, with constant bottom included; x-axis is the along-shore coordinate and the seawards direction is $y \to \infty$.

Boussinesq approximation of density ρ, the governing equations become

$$\frac{\partial \vec{v}_h}{\partial t} + \vec{v} \cdot \nabla \vec{v}_h = -f\vec{k} \times \vec{v}_h - \frac{1}{\rho_r}\nabla_h p + \frac{\partial}{\partial z}\left[\frac{\vec{\tau}_h}{\rho_r}\right],$$

$$\begin{aligned} \frac{\partial p}{\partial z} &= -\rho g, \\ \frac{\partial \rho}{\partial t} + \vec{v} \cdot \nabla \rho &= 0, \\ \nabla \cdot \vec{v} &= 0, \end{aligned} \tag{2.25}$$

where, $\vec{u}$ is the velocity vector, p is pressure, $f > 0$ is the Coriolis parameter, $\vec{\tau}_h$ is the horizontal turbulent stress, and ρ_r is a constant density. We take there is no friction from atmosphere. The mean horizontal Lagrangian transport $(\bar{U}_L, \bar{V}_L)$, correct to second order in wave steepness, is obtained by integrating the governing equation in vertical between the bottom and the moving surface. Mean horizontal volume fluxes are defined as (2.14). As discussed in previous sections, the mean horizontal Lagrangian flux is Stokes flux plus mean Eulerian flux (*Phillips*, 1966). We consider trapped internal Kelvin waves, which is generated by small perturbations

of stratification from its state of rest, traveling in along-shore direction. Introducing the vertical displacement of the isopycnals from their original position and Brunt-Väisälä frequency $N^2 = -gd\rho_0(z)/(\rho_r dz)$, the linearized equations for internal Kevin waves is obtained from (2.25). The variables may be separated into normal modes (*Lighthill*, 1969; *Gill and Clarke*, 1974). By inserting pressure normal modes into linearized momentum equation in z-direction, it is easy to show that the eigenfunctions ϕ_n are solutions of

$$\phi_n^{''}(z) + \frac{N^2}{c_n^2}\phi_n(z) = 0, \tag{2.26}$$

where, c_n is the constant eigenvalue. Assuming a rigid lid at the surface, i.e. $\phi_n = 0$, at $z = -H, 0$, that eigenfunctions $\phi_n^{'}$, constitute an orthogonal set for arbitrary Brunt-Väisälä frequencies. Utilizing the orthogonality condition and modeling the friction by a turbulent coefficient of momentum ν_T (*Williams and Gibson*, 1974), we find the governing equations for mode n, where the along-shore linear wave velocities and wave amplitudes must be vanished as $y \to \infty$. The resulting linear internal coastal Kelvin wave motion for mode n becomes

$$\bar{\xi} = \sum_{n=1}^{\infty} \xi_n(x, y, t)\phi_n(z). \tag{2.27}$$

Here

$$\xi_n = \xi_{0n} \exp(-\alpha_n x - a_n^{-1} y) \cos(k_n x + l_n y - \omega t), \tag{2.28}$$

where, α_n and k_n are spatial decay rate and wave number in along-shore direction, respectively. Furthermore, a_n and l_n are the internal Rossby radius and the friction-induced wave number in the y-direction, respectively. We note that the co-phase lines are slanted backwards for spatially damped coastal Kelvin waves. It is shown that the associated Stokes volume flux for internal coastal Kelvin waves is zero. Therefore, in this problem, the mean Eulerian volume flux is determined entirely by mean Lagrangian flux:

$$\bar{U}_L = \bar{U}_E, \qquad \bar{V}_L = \bar{V}_E. \tag{2.29}$$

Hence, the mean Eulerian velocities can be determined to second order in wave steepness from (2.25).

Chapter 3

Observations

3.1 The Caspian Sea

The Caspian Sea (CS) is the largest inland water body of the world with a surface area of 379000 km^2, a drainage area of approximately 3.5 million km^2, and a volume of $78000\,$km^2 (*Ghaffari and Chegini*, 2010; *Zaker et al.*, 2007, 2011). This lake is located at northern hemisphere between latitudes of 36° and 45°. Conventionally southern, central and northern basins are distinguished. The Southern and the central basins of the CS have maximum water depths of 1025 and $788\,$m, respectively. These basins are separated by a sill with a maximum depth of about $170\,$m and the northern basin with maximum depth about $20\,$m is a very thin extension of the central basin. The f/H contours in the Caspian Sea are indeed closed in both the central and southern basins (Fig. 3.1).

The vertical structure and evolution of the density field is a function of both salinity and temperature. Salinity in the CS is relatively constant with depth, and the density gradient can be to a first approximation considered proportional only to the temperature gradient. In the southern basin, the surface densities are significantly weaker, producing larger near-surface gradients (*Ghaffari et al.*, 2010, 2013). The process of hydrological fields transformation, redistribution of biogenic and pollutant substances depends significantly on horizontal circulation of the CS, which for different reasons have not been studied enough (*Ghaffari and Chegini*, 2010). Main circulations in the CS consist of cyclonic eddies (*Terziev et al.*, 1992) and meso-scale eddy features which have seasonal evolution (*Trukhchev et al.*, 1995). Due to lake of tide, the CS currents are considered to be mainly wind-generated. Wind and traveling weather fronts transfer momentum directly as wind driven currents and indirectly by triggering different sort of surface and internal waves. For instance, the periodic occurrence of rip currents and formation of cusp-type beach, which are indications of edge waves on natural shorelines (*Bowen and Inman*, 1969, 1971), were stated by *Sonu et al.* (1969) in the CS . Furthermore, pronounced vertical stratification in the southern basin (*Ghaffari et al.*, 2010) along with straight coast, make that coastal region favorable for internal wave generation and propagation. Other types of currents, e.g. baroclinic currents and seiches also play important roles in local circulation patterns (*Sur et al.*, 2000). Over the central and southern basins of the CS, the main features of circulation are a cyclonic (*Ghaffari and Chegini*, 2010). Although various field measurements were carried out in the northern and the central basins of the CS (*Bondarenko*, 1993, 1994; *Kosarev*, 1975),

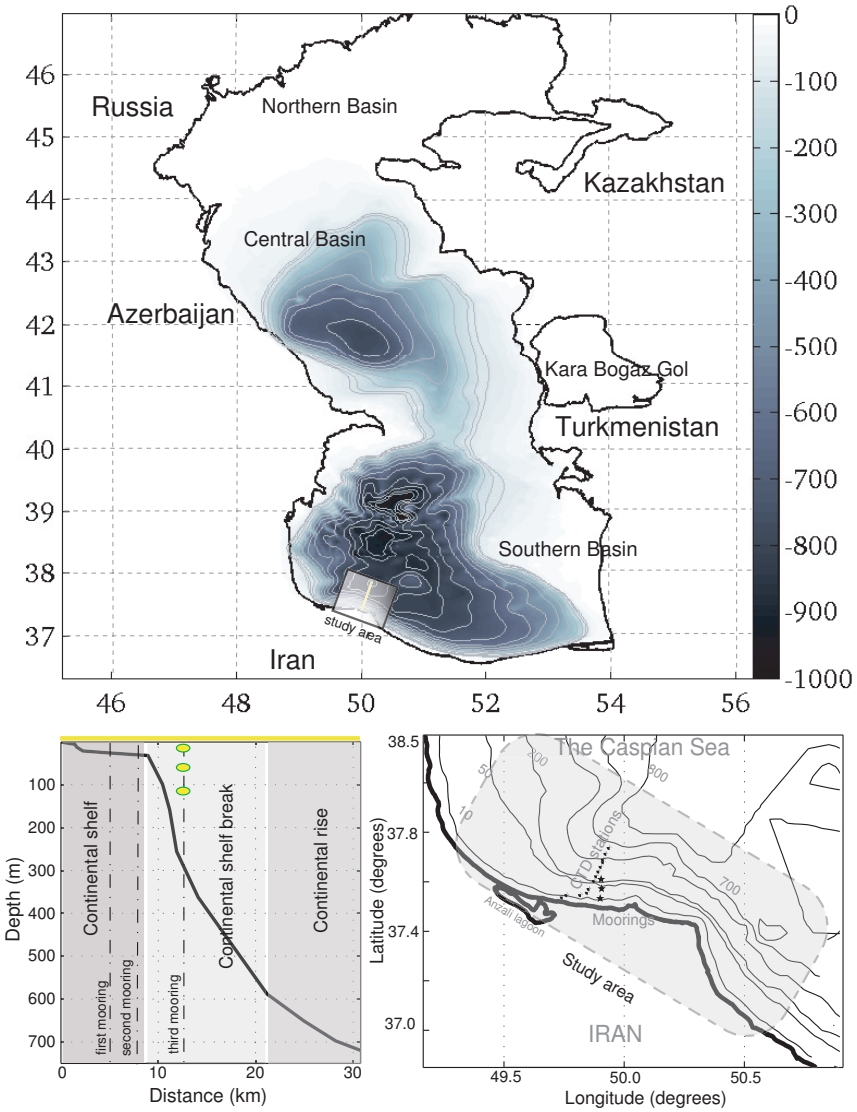

Figure 3.1: The Caspian Sea; upper panel: the bathymetric field (shown as gray shading), and potential vorticity field (contours); lower panel: shelf profile and location of field observations.

but only a few number of measurements in order to investigate the coastal flow field have been accomplished in the southern basin direct (*Ghaffari and Chegini*, 2010; *Ghaffari et al.*, 2010, 2013; *Zaker et al.*, 2007, 2011).

3.2 Field measurements

3.2.1 Study area

The study area is located in the southwestern part of the CS (Fig. 3.1). The depth decreases gently from the coast to approximately -50 m near the shelf break in almost 10 km, after that it sharply decreases to ~ 800 m in 25 km. According to the bathymetric features, the continental shelf spreads from the coast up to about 10 km seaward with mild declination, which ensues by a drastic depression (the continental shelf break) extends to 20 km seaward and hits its lowest point at 600 m (Fig. 3.1). The continental rise commences from this point and goes down with a relatively mild slope with respect to the continental shelf break toward the abyssal plain . The continental shelf in the southern coastal areas is fairly narrow and topographic contours are parallel to the coastline (*Ghaffari et al.*, 2010; *Ghaffari and Chegini*, 2010; *Zaker et al.*, 2007).

3.2.2 Satellite observations

Satellite observations (from January 1992 to December 2011, available at www.aviso.com) are utilized to study the basin-scale spatial and temporal variations of Sea Level Anomaly (SLA) in the CS. We use empirical orthogonal function (EOF) analysis to extract coherent variations that are dominant, i.e. possible spatial modes of variability and how they change with time. Utilizing that procedure, the spatial-temporal anomalies of the dataset is decomposed into its leading patterns. In fact, by computing the eigenvalues and eigenvectors of a spatially weighted anomaly covariance matrix of a field, the leading patterns in both time (Principal Component, PC) and space (EOF) are determined.

The leading orthogonal function (EOF1) is remarkably similar to the f/H field in the central basin. However, in the southern basin the the response is less clear. The first principal component (PC1), the time series associated with EOF1, accounting for 92% of the total variance in the SLA field. The remaining higher EOFs account for only 8% of the variance, which are less likely to be effective in dynamical posses of the basins (Fig. 3.2). As may one can expect, the northern shallow extension of the CS display entirely separate pattern mostly under the influence of the Volga River runoff.

3.2.3 Current meter observations

Three moorings were deployed in a line perpendicular to the coastline from November 2004 to early May 2005, in order to record the flow field over the south-western shelf of the CS . The moorings were located over the 20 m, 50 m and 230 m isobaths at [$37.505\,^{\circ}$N; 49.865°E], [37.531°N; 49.866°E], [37.553°N; 49.864°E], respectively. Recording Current Meters (RCM 9) were installed near the surface, mid-depth (for the 230 m mooring), and near the bottom, aiming to provide current profiles throughout the water column. In order to capture fine details of the

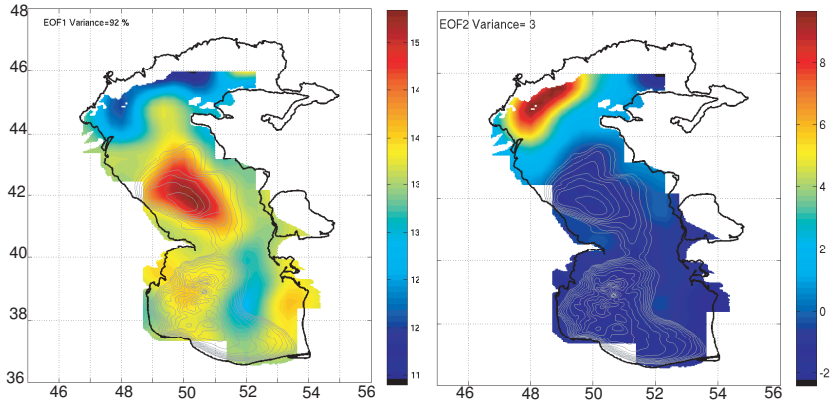

Figure 3.2: EOF analysis of SLA for the CS over f/H contours. Leading (right) and second (left) EOFs, which accounts for 92% and 3% of total variance in the field, respectively.

flow field, the sampling frequency was originally set to 3 cph. However, the analysis presented here is based on daily averaged time series. Furthermore, the currents were decomposed into along-shore and cross-shore components based on their principal axes. Figure 3.3 shows the along-shore daily averaged current time series for the three moorings. The first two moorings, located on the continental shelf, demonstrate barotropic behavior of the flow field. In the third mooring, strong temporal variations in the flow field corresponding to low frequency motions were captured by all the current meters. However, relatively high frequency signals are not well captured by the lower current meter. The latter instrument was located far below the seasonal thermocline layer. But, estimates of the squared coherences among the current time series of this mooring at various timescales, show high correspondence at periods longer than several days. Therefore, the low frequency fluctuations have appreciable vertical coherence. We use this mooring for further analysis, as it provides a better perspective of the velocity structure in the basin interior.

Our analysis show that the depth averaged velocity accounts for $\sim 85\%$ of the total velocity variance in the study area. Additionally, variance ellipses are formed in order to study the topographic influence on the velocity field. The current ellipses at all depths are anisotropic, and the principal axes of the variabilities are closely aligned with ambient topographic contours in all three moorings. This implies the tendency of the flow to be steered along the topographic contours in the study area. This results are consistent with previous studies which showed the alignment of current ellipses with topographic contours, and almost barotropic (equivalent barotropic) behavior of the flow field in the eastern part of the southern CS (*Ghaffari and Chegini*, 2010; *Zaker et al.*, 2011).

3.2.4 Hydrographic observations

A total of 13 CTD-profiles along a transect extending from the coast towards the offshore region, as shown in Fig. 3.1, were carried out in the early winter and summer of 2008. The stations

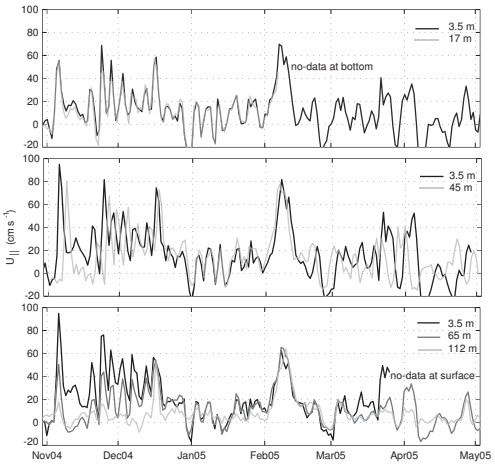

Figure 3.3: Along-shelf currents; first–third mooring from top to bottom respectively for 6 months (November 2004–May 2005). The light gray and black lines show daily averaged velocities for top and bottom current meters, respectively. The dark gray line in the lower panel represents mid-depth observation. Note how nearly barotropic the currents are in the all three stations.

were selected based on the bathymetric contours in approximately 3 km intervals to cover some specific depths along the study area. The first station located at [$37°29.185'$ N; $49°27.959'$ E] and the last one located at [$37°44.121'$ N; $49°40.470'$ E], which hits its lowest point at ~ 750 m depth. According to the bathymetric features, the profiled stations well covered the deepest parts of the south-western waters and could be representative for deep water characteristics in this region. Figure 3.4 shows potential density and temperature structures in the study area based on snapshot hydrographic observation. It reveals strong seasonal thermocline located at ~ 30 m depth, which is typical seasonal thermocline depth in summer for almost whole basin (*Ghaffari et al.*, 2013). Contrary to the strong summer thermocline in southern part of the CS, the water body in the cold phase over the continental shelf break is partially ventilated. Owing to the cold phase erosion, the seasonal thermocline inevitably sinks down to the deeper layers and is located between 80 to 100 m depth, where the water mass is still stratified. As it mentioned before, due to insignificant vertical salinity variation in the CS, temperature structure largely determines the density stratification. Therefore, density stratification is weaker but does not vanish in winter (*Terziev et al.*, 1992; *Kosarev*, 1975; *Ghaffari et al.*, 2010). These observation suggest that the vertical stratification may be important in the study area. Therefore, an equivalent barotropic description of currents seems appropriate. Taking into account the near barotropic structure of the velocity field and presence of a permanent stratification in the southern basin, one can expect that a simplified EB model of wind-driven variability be applicable in this region.

The permanent and profound stratification along with a straight coastline, makes the southern coastal region of the CS an ideal environment for internal Kelvin waves. In general, our understanding of wind-generated surface waves are considerably developed due to the exchange between proper argued theories and careful and extensive observation. However, internal waves studies are lacking in similar prolific interchange not because of the complexity of the problem,

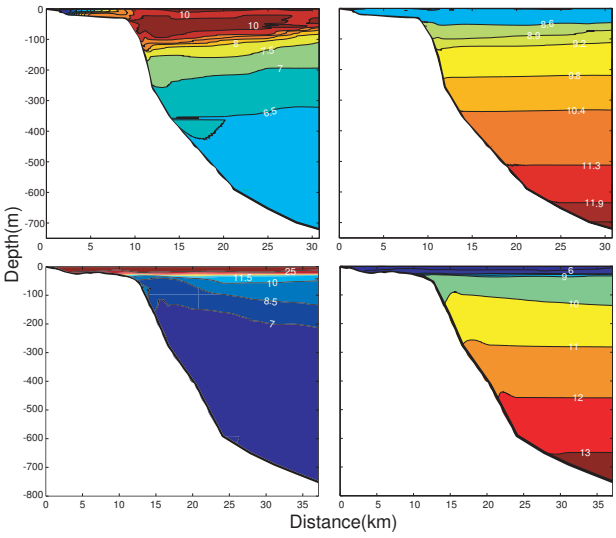

Figure 3.4: Temperature (left) and density (right) structures of the south-western part of the CS for cold (upper) and warm (lower) phases in 2008 (*Ghaffari et al.*, 2010).

but due to difficulty of making significant measurements. Variations in water temperature and salinity at a fixed point depth have often been attributed to internal waves (*Phillips*, 1966). In order to investigate internal waves in the study area, the third mooring was equipped by thermistor chains. Figure 3.5 shows vertical profile of temperature time series from surface to $120\,\mathrm{m}$

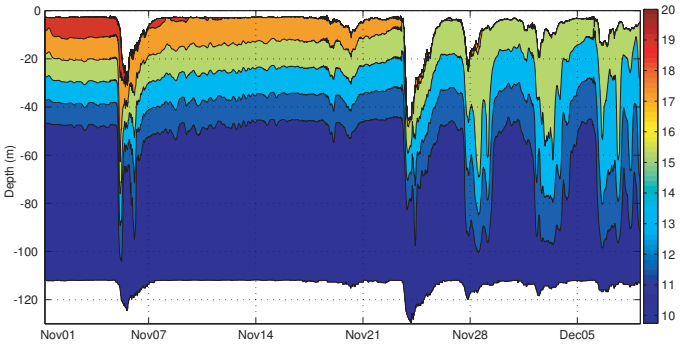

Figure 3.5: Time series of isotherm fluctuations in the south-western part of the CS.

depth. The fluctuation with a period of about 5 days can be considered as indication of internal Kelvin waves. Although little is known about the distribution of the energy among the different internal waves mode, in fairly sharp thermocline the gravest mode may dominate (*Phillips*, 1966). In view of the considerably sharp thermocline in the CS, one may attribute the vertical amplitude of the fluctuations $\sim 40\,\mathrm{m}$ to a first mode internal wave.

In summary, the CS with its bottom contours, sloping beaches and stratification appears to exhibit, or be capable of exhibiting the wind and wave-driven current phenomena discussed in this thesis.

Chapter 4

Results

In the previous chapters, we provided an explanation of why and how our research for each thesis objective was conducted. The results of the research will be addressed briefly in this chapter, and a short discussion of the results will follow. The detailed investigation of each objective and its results are mainly presented in the individual papers.

4.1 Topographic Effects on the Large-scale Flow Field in the Caspian Sea

The barotropic and EB models which are described in chapter 2 are relevant in regions where PV contours are closed. Such models have been used before to investigating wind-driven variability (*Isachsen et al.*, 2003; *Hasselmann*, 1982; *Killworth*, 1992; *Krupitsky et al.*, 1996; *Kamenkovich*, 1962). In this model, the primary component of the flow is parallel to the PV contours. The flow is forced by wind-driven Ekman divergence at the surface and balanced by frictional Ekman convergence at the bottom. As shown in the Fig. 3.1, the PV contours are indeed closed in both the central and southern basins of the CS, and some of them cover both basins. Satellite observation of SSH (Fig. 3.2) show that variability is localized in the basins; this is particularly true in the central basin. *Isachsen et al.* (2003) found that SSH variability was similarly localized in the gyres of the Nordic Seas, and there the f/H model successfully captured a large fraction of the observed variability. Furthermore, in-situ velocity field observations show that the principal axes of the variabilities are closely aligned with ambient PV contours in all three moorings. Therefore, the tendency of the flow to be steered along the topographic contours in the study area, is evident. Despite to the Ekman flux in the surface layer, the flow varies in correspond with the topographic variations, which supports the idea of investigating the role of the topography in controlling the barotropic flow in the CS. In the following, the barotropic linear model will be tested in these basins.

For the atmospheric forcing, we utilized almost 20 years (1992–2011) of wind stress data from the European Centre for Medium-Range Weather Forecasts (ECMWF) operational analysis (available online at http://www.ecmwf.int). The transfer of the atmospheric momentum to the sea can be altered by the sea surface ice coverage but the central and southern parts of the CS are ice-free basins. Bathymetry data for the CS were obtained from the ETOPO2 $(2' \times 2')$ topographic set (available online at http://www.ngdc.noaa.gov). For application in a linear model

of the large-scale flow this topographic data set needs some smoothing, at the same time, excessive smoothing of topographic gradients will lead to underestimated flow strength. However, it is not that straightforward to define the appropriate smoothing scale. In fact, the PV contours can be changed (broader or denser) or disappear with different smoothing bands (*Krupitsky et al.*, 1996). After some testing, we defined the large-scale component of the topography by smoothing the bathymetry to ~ 10 km in both latitudinal and longitudinal directions, at $40°$N.

We first compared the predicted velocity over the closed PV contours with in-situ current observations, i.e., with currents at the deepest mooring there. The other two moorings are in the vicinity of the third one and demonstrate very similar velocity field. The upper panel in Fig 4.1 shows the predicted along-PV currents at the mooring location. The model produces seasonal variation of the mean currents with maximum values in the winter times. Also shown here is the duration of the in-situ current observation in the study area. The lower panel, shows the observed depth-averaged currents against the barotropic model predictions for this period. It is evident that most of the high frequency signals are not captured by the model. Some of the observed low-frequency variations (> 1 month) are captured. But the model predictions are broad and systematically underestimate the observed currents. In fact the model appears to act like as low-pass filter. In order to achieve a proper agreement between the observation and prediction amplitude, we had to use bottom friction coefficient $R = 1 \times 10^{-4}\,\mathrm{m\,s^{-1}}$, a value five times lower than the drag coefficient was used by *Isachsen et al.* (2003). From 2.5, it is easy to see that smaller R values maintains higher amplitudes. On the other hand, small bottom drag coefficient makes $i\omega$ more dominant, which smooths out the predicted current and causes phase shift. Therefore, we expect the high frequency signals are filtered out in our predictions. We see

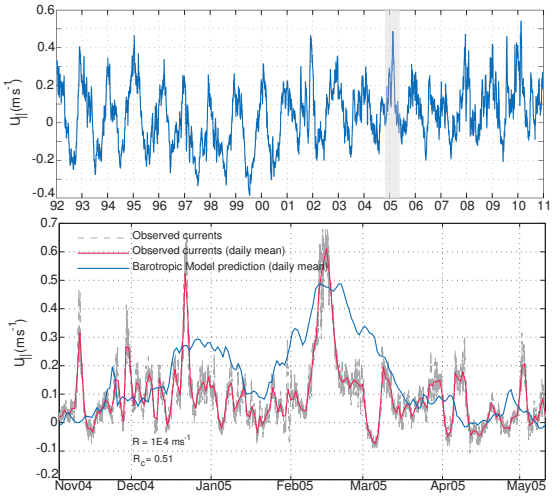

Figure 4.1: The upper panel; the along-PV predicted current (1992–2011). The gray shaded area shows the length of the in-situ current observation. In the lower panel, the gray dashed, red and blue solid lines show the depth-averaged along-PV current based on the recorded (6 cpd), daily mean time series, and the barotropic model prediction, respectively.

some skill and some problems of the model, but really need more observations to learn more. Considering the measurements durations, we do not have sufficient amount of supporting data,

and the comparison is inconclusive. Therefore, we look at altimetry observation. The spatial and temporal structure of the large-scale flow is well captured by satellite altimetry. We compare sea surface height anomalies among two transects over closed PV contours in the central and southern basins of the CS (see Fig. 4.2). The sea level variations between the inner and

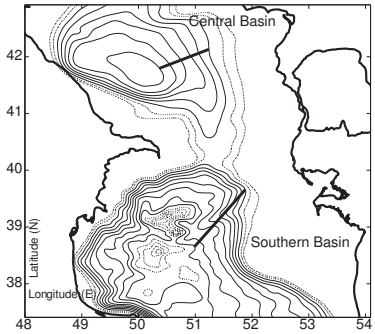

Figure 4.2: Shown in the current figure are the two gyres (in the central and the southern basins) for which the differences in sea level anomalies between satellite observations and model predictions, were compared. The thick lines indicate the integration paths, as well as the outer and inner PV contours. The latter is considered for determining the sea level anomalies for satellite observations.

outer contours are determined using weekly multi-satellite altimetry data from October 1992–December 2010. For model comparison, sea surface anomalies in the southern and the central basins over the sub-basin PV contours (the basin-wide contours were excluded) are predicted in the barotropic equation (2.6). The central region of the southern basin is too flat. In fact, small ups and downs in that region forms several closed cores, and PV contours are rather convoluted. Therefore, we limit our calculations to the continental slope. The barotropic model behaves quite different in the southern and central sub-basins. While the model predicts the sea surface height anomalies relatively well in the central basin, the model performance diminishes in the southern basin (Fig. 3.3). The satellite observations in the central basin reveals seasonal variation with lowest values in winters. This seasonal signal is captured very well by the barotropic model. However, in the southern basin neither the observation nor the model show any clear seasonal cycle. The linear correlation coefficients between the satellite measurements and the barotropic model prediction in the central and the southern transects, are 0.68; 0.51, respectively . The ratio of the RMS of the predicted SLA to the RMS of observed SLA for the central and the southern basins are 0.8 and 0.3, respectively. Ergo, despite the better performance of the model in the central basin, in both cases the predictions are underestimated.

In the barotropic model, the bottom topography is dominant. Weak stratification and equating the surface and bottom velocities to the depth-averaged velocity are bases for preeminent topography in the barotropic solution. In fact, the topographic steering depends on both the stratification and strength of the bottom currents. The topographic steering is attenuated by the stratification, since the velocity decreases from the surface to the bottom in a stratified water body. Additionally, the potential density distribution reveals that the southern basin is more stratified comparing to the central basin. A measure of the relative importance of stratification and rotation within a flow field is the Burger number. Estimations of the Burger number for

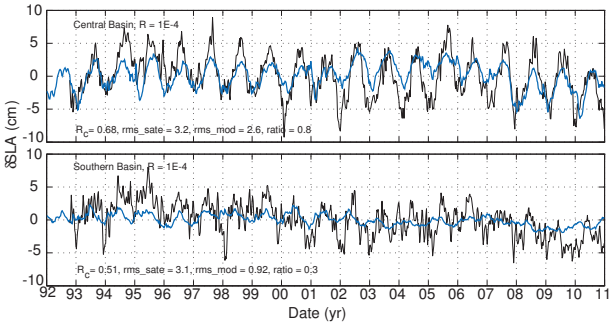

Figure 4.3: Time series of the relative sea level displacements between the rim and the inner PV contours in the two different transects over the central and the southern basins gyres of the CS. The black and blue lines indicate weekly time series of the sea level anomalies based on the satellite observation and the barotropic model prediction, respectively.

southern and central basins (considering a horizontal length scale as $50\,\mathrm{km}$), are $0.057;\ 0.027$, respectively. In both cases, the Burger number is less than 1, but the stratification is stronger in the southern basin. The observations show that the velocities in the lower layers are smaller than the velocities in upper layers, but in the same direction (see, Fig. 3.3). Therefore, the velocities are parallel, but decay with depth. This implies that, an equivalent barotropic (EB) model may be applicable in the southern basin.

We examined different e-folding scale (h_0) values in the central and the southern basins, to achieve the best agreement between satellite measurements and EB model. For the EB model, we used the same bottom drag coefficient as *Isachsen et al.* (2003) applied for the Nordic Seas and Arctic Ocean ($R = 5.0 \times 10^{-4}\,\mathrm{m\,s^{-1}}$). The best agreement between observation and EB model in the central basin occurs at $h_0 = 800\,\mathrm{m}$. Although, the correlation coefficient is same as the barotropic model, the amplitude remarkably is improved. Additionally, the ratio of the RMS of predicted SLA to the RMS of observed SLA for the central basin is increased from 0.8 to 1.1. In the southern basin, the EB model shows high accordance with observation at $h_0 = 500\,\mathrm{m}$. The correlation coefficient between observation and prediction is modified from 0.51 (barotropic model) to 0.58, also the amplitude is considerably improved. The RMS ratio enhancement from 0.3 to 0.7 shows that, despite the barotropic model, the EB model predictions are not extremely underestimate in the southern basin. Note, we used five times stronger drag coefficient in the equivalent model than the pure barotropic one. Although, the stronger drag coefficient decreases the amplitude, but $P(-H)$ is small when $H \gg h_0$, which reduces the drag coefficient and, maintains the amplitude. In some studies an augmentative constant has been introduced, to obviate the reducing effect of $P(-H)$ (see, *Krupitsky et al.* (1996); *Ivchenko et al.* (1999)). In line with *LaCasce and Isachsen* (2010), we did not apply that constant, and apparently, the performance of the model in terms of the amplitude is acceptable. In fact, the drag could be too weak, if the depth largely exceeds h_0. In such a configuration, the wind forcing is essentially unbalanced. Taking into account the best e-folding scale and maximum depth, the large depth condition ($H \gg h_0$) never fulfills in the CS. Therefore, the drag is not that weak in this problem. Additionally, the stronger drag coefficient makes the $i\omega$ less dominant and reduces its filtering effect. As one might expect, the EB model renders relatively better

performance in capturing of the high frequency signals. For more detailed discussions about the application of the EB model in the CS, see paper I.

4.2 Mass transport in the Stokes edge wave for constant arbitrary bottom slope

In this study we investigate the nonlinear mass transport in the Stokes surface edge wave in an unbounded ocean. This is done by applying an Eulerian description of motion, and expanding the solution in series after wave steepness as a small parameter. We derive analytical expressions for the vertically-averaged Lagrangian drift velocity induced by Stokes edge wave in a rotating and non-rotating ocean. This drift is composed of Stokes drift plus Eulerian velocity.

We derive analytical expressions for the total mean energy (E), and total dissipation rate (D), from linear wave solution. Following *Gaster* (1962) and transition from temporal damping to spatial damping, an expression for the spatial attenuation coefficient is obtained. It is shown that the non-rotating case can be recovered by setting $f = 0$, in the rotating expression. It was demonstrated by *Longuet-Higgins and Stewart* (1960) that the radiation stress (S) forcing would be $\frac{1}{2}(-\partial E/\partial y)$ for deep water waves and $\frac{3}{2}(-\partial E/\partial y)$ for shallow water waves in a non-rotating ocean for constant depth. For Stokes edge waves, the time rate of change of the total Lagrangian momentum flux in the wave direction is forced by the divergence of the total energy density $-\partial E/\partial y$, in both rotating and non-rotating cases.This value is mid-way between the deep and shallow water values. Since the particles move in planes parallel to the sloping bottom, there is a cross-wave velocity component. This transverse velocity contributes in wave energy, but does not appear in the radiation stress term. Hence, one would expect a relation that differs from that of *Longuet-Higgins and Stewart* (1960). Therefore, the wave energy in the entire trapped zone yields $\int_0^\infty S dx = E/\rho$. This is exactly same for the rotating and the non-rotating Stokes edge wave, demonstrating that it is not the rotation, but the sloping bottom that yields a value which is in between the deep and shallow water values of *Longuet-Higgins and Stewart* (1960).

For a reasonable value of wavelength ($\lambda = 1\,\mathrm{km}$), for wave traveling with the coast to the left ($\omega > 0$), the critical slope angle becomes $\beta^* = 89.9°$, which is very close to the vertical wall limit. Hence, in practice, our calculations are valid in the interval $0 < \beta < \pi/2$ for the chosen wavelength. In Fig. 4.4 we have displayed non-dimensional Eulerian velocity and non-dimensional Stokes drift for various values of the bottom slope for ($\lambda = 1\,\mathrm{km}$). The results show that for larger slope angles, the trapped zone is wider for non-dimensional Eulerian drift. The calculations show that the Stokes drift and the Eulerian current have their maximum values at the shore line. The spatial variation over the shelf for non-dimensional Stokes drift and Eulerian current is almost similar for small and moderate slope angles. But, at the shore line it mainly depends on the slope angle. The ratio between the mean Eulerian current and the Stokes drift at the the shore is

$$\frac{v_{E0}}{v_{S0}} = Rk\sin\beta\left[1+\frac{1}{2}\left(\frac{f\omega}{gk}\right)^2\right], \tag{4.1}$$

where, R is friction. Therefore, for wave motion in which the earth's rotation becomes important, we see that increasing values of the Coriolis parameter, increase the Eulerian currents for

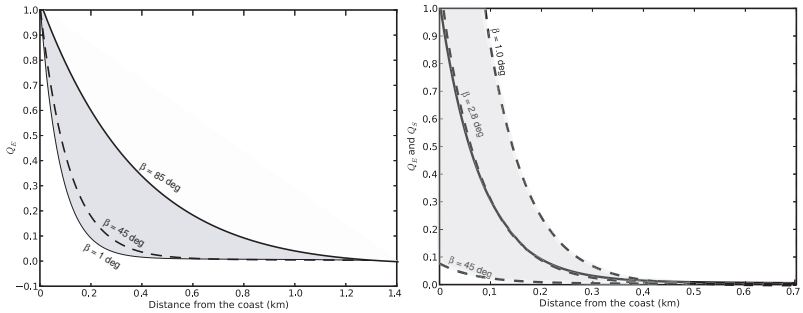

Figure 4.4: Non-dimensional Eulerian mean current Q_E (left) and non-dimensional Stokes drift current Q_S (right) for $\lambda = 1\,\mathrm{km}$.

a given bottom slope. For the wavelength considered here ($\lambda = 1\,\mathrm{km}$), the last term in the in the parenthesis is negligible. Therefore, the relative strength of the Eulerian current and the Stokes drift depends on friction and bottom slope. As the frictional influence should be of order unity, the slope angle plays vital role here. Hence, the relative importance of the mean Eulerian current to the Stokes drift can be expressed as $v_{E0}/v_{S0} \propto \sin\beta$. This demonstrate that for given wavelength, the Stokes drift tends to dominate the Eulerian current for small and moderate slope angles (see Fig. 4.4).

The theory developed here is valid for steeply sloping bottoms and our calculations for $\omega > 0$ are valid for all $\beta < \beta^*$. Such solutions may be convenient for comparison with experiments in wave tanks, where a steep slope may be advantageous. But, in natural environments beach slopes are mostly quite gentle. In order to relate our theoretical results to the natural environments, we consider the CS as a case study. In the southern basin of the CS the depth increases slowly from the coast over the continental shelf (see Fig. 3.1). As noted before, in such case the Stokes drift exceeds the mean Eulerian velocity. In this example, we take that the wave amplitude η_0 is $0.1\,\mathrm{m}$, the wavelength λ is $1\,\mathrm{km}$ and $f = 8.86 \times 10^{-5}\,\mathrm{s}^{-1}$. Furthermore, $\beta = 0.25^\circ$ is typical slope angle for the southern CS beach. By taking typical values for the linear friction coefficient ($K = 10^{-5}\,\mathrm{m\,s}^{-1}$), and eddy viscosity ($\nu = 10^{-3}\,\mathrm{m}^2\,\mathrm{s}^{-1}$), we obtain that $R = 10^2\,\mathrm{m}$ in this problem. For this est of parameters, we find $v_{E0} = 0.6\,\mathrm{cm\,s}^{-1}$ and $v_{S0} = 5.5\,\mathrm{cm\,s}^{-1}$ for the CS. We note that the Stokes drift is dominating component of transport and is comparable to traditional wind surge velocities. In the present study, the basis of the derivation of the fluxes is expressing the solutions as expansions in power series after the wave steepness as a small parameter. Hence, we must require that the second order Stokes drift must be considerably smaller than the linear velocity field. Consequently, the Stokes drift must be smaller than phase speed of the wave, which leads to $\eta_0 k < \sin\beta$. Here, we have $\eta_0 k = 6.28 \times 10^{-4}$, and $\sin\beta = 4.36 \times 10^{-3}$, which fulfills the condition quite well. Figure 4.5 shows phase speed ($c_p = \omega/k$) and Stokes drift velocity for the CS example. As it shown, for the chosen parameters, the Stokes drift is remarkably smaller than the phase speed, which indicates that the nonlinear theory is valid. For same configuration the Stokes drift velocity exceeds phase speed for waves with wave numbers larger than $k > 0.043\,\mathrm{m}^{-1}$, where the nonlinear theory is not valid. We note that different values of slope angle and wave amplitude can alter the Stokes drift. E.g. for larger bottom angles the Stokes drift velocity becomes smaller. Hence, for

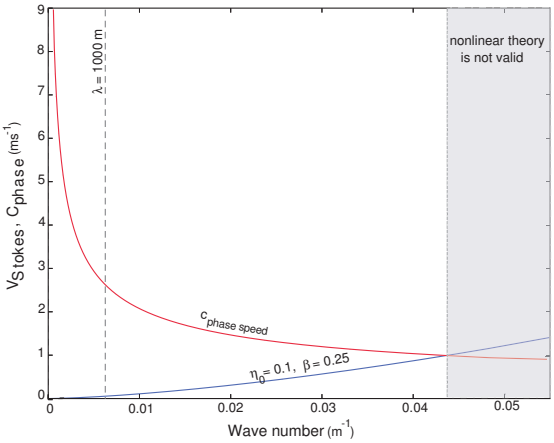

Figure 4.5: Dimensional Stokes velocity v_{S0} (blue line) and phase velocity c_p (red line) for Stokes edge waves for the southern Caspian beach; $\eta_0 = 0.1\,\mathrm{m}$, $\lambda = 1\,\mathrm{km}$, $f = 8.68 \times 10^{-5}\,\mathrm{s}^{-1}$ and $\beta = 0.25°$.

steeper bottom, the nonlinear theory is valid for even larger wave numbers. Conversely, wave amplitude plays significant role in increasing the Stokes drift velocity, which decreases wave number threshold for validity of the nonlinear theory.

Moreover, we consider two more locations; Slapton Beach (*Huntley and Bowen*, 1973), and Lake Michigan (*Donn and Ewing*, 1956), where we find short and long waves, respectively. In both cases the depth increases slowly. As we noted before, in such cases the Stokes drift is comparable to or exceeds the mean Eulerian velocity. For more detailed discussions about the Stokes edge wave-induced mass transport in aforementioned areas, see papers II and III.

4.3 Mass transport in internal coastal Kelvin waves

In the present study we have investigated the drift due to internal coastal Kelvin waves. We find the Stokes drift trapped to the coast within the Rossby radius of deformation. However, by integration in vertical, and application of proper boundary conditions, it is demonstrated that the associated Stokes volume flux for internal coastal Kelvin waves is zero. In line with this important result, the total mean Lagrangian transport attributes to only mean Eulerian transport. The mean Eulerian current for each mode is trapped to the coast within the Rossby radius of deformation, and that current is always positive (directed along the wave). Additionally, in a balanced flow the ratio of forcing from the wave field (through the radiation stress) and the restraint of bottom friction on the mean flow should be of order unity. The present approach yields the Stokes drift as function of depth, while the mean Eulerian current is determined as a depth average by integration from the bottom to the surface. This procedure masks the vertical variation of the Eulerian drift current, and makes comparisons with the Stokes drift at a certain depth difficult.

As an example for the Stokes drift in the internal coastal Kelvin waves, we consider the continental shelf break of the CS (see Fig. 3.4). In order to obtain the eigenvalues c_1, c_2, c_3

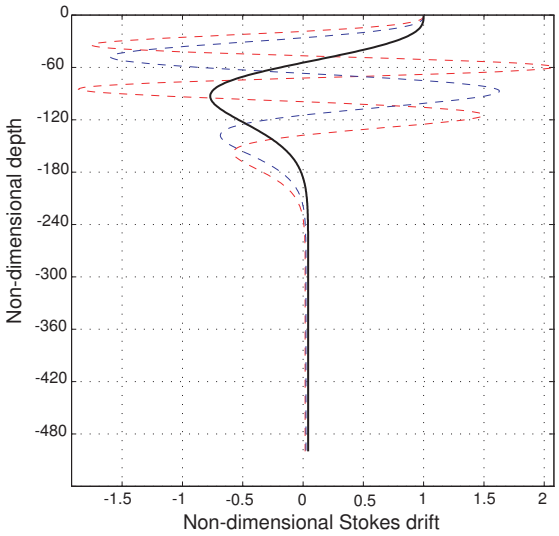

Figure 4.6: Non-dimensional Stokes drift for the first (dark line), second (blue dashed line), and third (red dashed line) baroclinic mode in the CS as function of non–dimensional depth.

etc., we must prescribe Brunt-Väisälä frequency in study area. Using measurements by *Ghaffari et al.* (2010) we find an expression for Brunt-Väisälä frequency, which is typical for winter condition in the south-western part. The eigenvalue problem is easily solved by a simple shooting procedure. We then obtain $c_1 = 1.21\,\mathrm{m\,s^{-1}}$. The next successive eigenvalues become $c_2 = 0.45\,\mathrm{m\,s^{-1}}$ and $c_3 = 0.28\,\mathrm{m\,s^{-1}}$ for the second and third baroclinic mode, respectively. The non-dimensional Stokes drift $\bar{u}_{Sn}/u_{0n}$ at the coast for first three successive baroclinic modes in the study area are shown in Fig. 4.6, where $u_{0n} \propto c_n \xi_{0n}^2$. Therefore, in dimensional form, wave amplitude and eigenvalue at each specific mode determine the Stokes drift value. We note that in the first baroclinic mode, the Stokes drift has its largest value at the coast, and reaches its largest negative value about $-80\,\mathrm{m}$, where the thermocline located and Brunt-Väisälä frequency has its maximum value (*Ghaffari et al.*, 2010). For fairly sharp thermocline, first mode mostly comprise a substantial portion of the total energy (*Phillips*, 1966). Hence, we particularly interested to the first mode, which we believe that contains majority of the energy fraction, considering almost sharp thermocline in the study area (Fig. 3.4). The isothermal contours fluctuation (Fig. 3.5) can be attributed to the first baroclinic mode of the internal Kelvin wave in the south-western part of the CS, since they both have almost the same period. Therefore, the measurements suggest a vertical amplitude of about $\xi_{01} = 40\,\mathrm{m}$ for the first baroclinic mode. This implies that the dimensional Stokes drift varies from $7\,\mathrm{cm\,s^{-1}}$ at surface to $-5\,\mathrm{cm\,s^{-1}}$ at the thermocline location. The negative and positive lobs of the Stokes drift depth profile fulfills the no-flux condition. However, the Eulerian flux is not zero, e.g. for first baroclinic mode, the Eulerian transport occurs within a narrow region of width $\sim 7\,\mathrm{km}$. Since the internal coastal Kelvin waves always propagate with the coast to the right (for $f > 0$), we conclude that there is a systematic contribution from such waves to the mean circulation in the CS. For more detailed discussions about the internal coastal Kelvin wave-induced mass transport in the study area, see

paper IV.

Chapter 5

Concluding remarks

This thesis discusses the topographic effect on wind-driven current variability as well as the mean currents due to topographically trapped waves. Through the individual papers, we investigate the wind-driven transport in regions with closed potential vorticity contours, and estimate the mean transport induced by trapped gravity waves such as the Stokes surface edge wave and the internal Kelvin wave. Such transports are interesting from a fluid dynamics point of view, but they also have practical implications. It is a fact that topographic changes in the ocean often are strongest close to the coasts or the shore line. Therefore topographically steered currents may advect effluents and pollution along coasts and beaches and thereby pose a threat to the coastal population. Furthermore, for small bottom sediments in suspension, this mean drift may contribute to beach erosion by relocating bottom material.

The mean drift velocity in progressive waves is not easy to observe using fixed point measurement. It is partly due to the nature of the Stokes drift, but also due to the small amplitudes which are easily masked by other dynamics, e.g. tidal and inertial currents. Lagrangian measurements, e.g. drifters, are needed to capture the mean wave-induced transport. On the other hand, a drifter also responds to the geophysical forcing by the wind, wind-waves, and the oceanic currents. It is therefore not straightforward to decompose the wave drift from the drifter motion. In this respect, the Caspian Sea as a tide-free, closed body of water seems a promising place for such experiments. This large lake can be regarded as prototype laboratory. During calm wind episodes, which are quite common in this region, the mean transport and drifter response may entirely be attributed to the remotely generated, transient waves. Here, a coupling of extensive numerical modeling with field observations would be quite profitable. Extracting the particle drift from the model output using a Lagrangian approach, and comparing it with Lagrangian observations would clearly improve our understanding of wave-driven currents.

Bibliography

Ardhuin, F., and A. D. Jenkins, On the interaction of surface waves and upper ocean turbulence, *J. Phys. Oceanogr.*, *36*, 551–557, 2006.

Blondeaux, P., M. Brocchini, and G. Vittori, Sea waves and mass transport on a sloping beach, *Proc. R. Soc. Lond.*, *458*, 2053–2082, 2002.

Blondeaux, P., G. Vittori, F. Bruschi, A.and Lalli, and V. Pesarino, Steady streaming and sediment transport at the bottom of sea waves, *J. Fluid Mech.*, *697*, 115–149, 2012.

Boehm, A. B., S. B. Grant, J. H. Kim, S. L. Mowbray, C. D. McGee, C. D. Clark, D. M. Foley, and D. E. Wellman, Decadal and shorter period variability of surf zone water quality at huntington beach, california, *Environ. Sci. Technol.*, *36*, 3885–3892, 2002a.

Boehm, A. B., B. F. Sanders, and C. D. Winant, Cross-shelf transport at huntington beach. implications for the fate of sewage discharged through an offshore ocean outfall, *Environ. Sci. Technol.*, *36*, 1899–1906, 2002b.

Bondarenko, A. L., *Currents of the Caspian Sea and formation of salinity of the waters of the north part of the Caspian Sea*, Nauka, Moscow, Russia, 1993, in Russian.

Bondarenko, A. L., Natural investigation of the Caspian Sea currents, *Russian Academy of Science, Water Problems Institute*, 1994.

Bowen, A. J., and D. L. Inman, Rip currents: 2. laboratory and field observations, *J. Geophys. Res.*, *74*, 5479–5490, 1969.

Bowen, A. J., and D. L. Inman, Edge waves and crescentic bars, *J. Geophys. Res.*, *76*, 8662–8671, 1971.

Charney, J. G., and A. Eliassen, A numerical method for predicting the perturbations of the middle latitude westerlies, *Tellus*, *1*, 38–54, 1949.

Donn, W. L., and M. Ewing, Stokes' edge waves in lake michigan, *Science*, *124*, 1238–1242, 1956.

Dore, B. D., Wave-induced vorticity in free-surface boundary layers: application to mass transport in edge waves, *J. Fluid Mech.*, *70*, 257–266, 1975.

Eckart, C., Surface waves in water of variable depth, *Wave Rept. 100, S.I.O. Ref. 51-12, 99 pp*, Scripps Institution of Oceanography, 1951.

Evans, D. V., Edge waves over a sloping beach, *Q. J. Mech. Appl. Maths.*, *42*, 131–142, 1989.

Gaster, M., A note on the relation between temporally-increasing and spatially-increasing disturbances in hydrodynamic stability, *J. Fluid Mech.*, *14*, 222–224, 1962.

Ghaffari, P., and V. Chegini, Acoustic doppler current profiler observations in the southern Caspian Sea: shelf currents and flow field off Feridoonkenar bay, iran, *Ocean Sci.*, *6*, 737–748, 2010.

Ghaffari, P., and J. E. H. Weber, Mass transport in the Stokes edge wave for constant arbitrary bottom slope in a rotating ocean, *J. Phys. Oceanogr.*, doi:10.1175/JPO-D-13-0171.1, in press, 2014.

Ghaffari, P., H. A. Lahijani, and J. Azizpour, Snapshot observation of the physical structure and stratification in deep-water of the south Caspian Sea (western part), *Ocean Sci.*, *6*, 877–885, 2010.

Ghaffari, P., P. E. Isachsen, and J. H. LaCasce, Topographic effects on current variability in the Caspian Sea, *J. Geophys. Res. Oceans*, pp. 1–10, 2013.

Gill, A. E., and A. J. Clarke, Wind-induced upwelling, coastal currents, and sea-level changes, *Deep-Sea Res.*, *21*, 325–345, 1974.

Gille, S. T., E. J. Metzger, and R. Tokmakian, Seafloor topography and ocean circulation, *Oceanography*, *17*, 47–54, 2004.

Gordon, A. L., E. Molinelli, and T. Baker, Large-scale relative dynamic topography of the Southern Ocean, *J. Geophys. Res.*, *83*, 3023–3032, 1978.

Greenspan, H. P., *The Theory of Rotating Fluids*, Breukelen Press, Brookline, MA, 1990.

Hasselmann, K., An ocean model for climate variability studies, *Prog. Oceanog.*, *11*, 69–92, 1982.

Howd, P. A., A. J. Bowen, and R. A. Holman, Edge waves in the presence of strong longshore currents, *J. Geophys. Res.*, *97*, 11,357–11,371, 1992.

Huntley, D. A., and A. J. Bowen, Field observations of edge waves, *Nature*, *243*, 160–162, 1973.

Isachsen, P. E., J. H. LaCasce, C. Mauritzen, and S. Häkkinen, Wind-driven variability of the large-scale recirculating flow in the Nordic Seas and Arctic Ocean, *J. Phys. Oceanog.*, *33*, 2534–2550, 2003.

Ivchenko, V., A. Krupitsky, V. Kamenkovich, and N. Wells, Modeling the Antarctic Circumpolar Current: A comparison of fram and equivalent barotropic model results, *J. Mar. Res.*, *57*, 29–45, 1999.

Jenkins, A. D., The use of a wave prediction model for driving a near-surface current model, *Deutsche Hydrografische Zeitschrift*, *42*, 133–149, 1989.

Kamenkovich, V. M., On the theory of the Antarctic Circumpolar Current, *Trudy Instituta Okeanologii*, *56*, 245–306, 1962.

Killworth, P. D., An equivatent-barotropic modein the fine resolution Antarctic model, *J. Phys. Oceanog.*, *22*, 1379–1387, 1992.

Kosarev, A. N., *Gidrologiya Kaspiiskogo I Aralskogo morey*, Moscow University Press, Moscow, USSR, 1975.

Krupitsky, A., V. M. Kamenkovich, N. Naik, and M. A. Cane, A linear equivalent barotropic model of the Antarctic Circumpolar Current with realistic coastlines and bottom topography, *J. Phys. Oceanogr.*, *26*, 1803–1824, 1996.

Kurkin, A., and E. Pelinovsky, Shallow-water edge waves above an inclined bottom slowly varied in along-shore direction, *Europ. J. Mech. B/Fluids*, *22*, 305–316, 2003.

LaCasce, J., and P. E. Isachsen, The linear models of the ACC, *Prog. Oceanog.*, *84*, 139–157, 2010.

Lamb, S. H., *Hydrodynamics*, sixth edition ed., Cambridge at the University Press, 1932.

LeBlond, P. H., and L. A. Mysak, *Waves in the ocean*, Elsevier Oceanog. Series, 20. Elsevier, Amsterdam, 1978.

Leichter, J. J., S. R. Wing, S. L. Miller, and M. W. Denny, Pulsed delivery of subthermocline water to Conch Reef (Florida keys) by internal tidal bores, *Limnolog. Oceanog.*, *41*, 1490–1501, 1996, n/a.

Lighthill, M. J., Dynamic response of the Indian Ocean to onset of the soutsouth monsoon, *Phil. Trans. R. Soc. London A*, *265*, 45–92, 1969.

Longuet-Higgins, M. S., Mass transport in water waves, *Phil. Trans. R. Soc. Lond.*, *A245*, 535–581, 1953.

Longuet-Higgins, M. S., and R. W. Stewart, Changes in the form of short gravity waves on long waves and tidal currents, *J. Fluid Mech.*, *8*, 565–583, 1960.

Marshall, D., Topographic steering of the Antarctic Circumpolar Current, *J. Phys. Oceanogr.*, *25*, 1636–1650, 1995.

McWilliams, J. C., P. P. Sullivan, and C. Moeng, Langmuir turbulence in the ocean, *J. Fluid Mech.*, *334*, 1–30 M3 – 10.1017/S0022112096004,375, 1997.

Mei, C. C., A note on the averaged momentum balance in two-dimensional water waves, *J. Mar. Res.*, *31*, 97–104, 1973.

Mok, K. M., and H. Yeh, On mass transport of progressive edge waves, *Phys. Fluids*, *11*, 2906–2924, 1999.

Nielsen, P., *Coastal Bottom Boundary Layers and Sediment Transport. Advanced Series on Ocean Engineering*, vol. 4, World Scientific, Singapore, 1992.

Nøst, E., Calculating tidal current profiles from vertically integrated models near the critical latitude in the Barents Sea, *J. Geophys. Res.*, *99*, 7885–7901, 1994.

Phillips, O. M., *The Dynamics of the Upper Ocean*, Cambridge University Press, New York, 1966.

Reid, R. O., Effects of coriolis force on edge waves. (i) investigation of the normal modes, *J. Mar. Res.*, *16*, 109–144., 1958.

Röhrs, J., K. H. Christensen, L. R. Hole, G. Broström, M. Drivdal, and S. Sundby, Observation-based evaluation of surface wave effects on currents and trajectory forecasts, *Ocean Dynamics*, *62*, 1519–1533, 2012.

Sonu, C., S. Murray, U. S. O. of Naval Research, L. S. University, Agricultural, and M. C. C. S. Institute, *Collective Movement of Sediment in Littoral Environment*, Coastal Studies Institute, Louisiana State University, 1969.

Stokes, G. G., Report on recent researches in hydrodynamics, *Rep. 16th Brit. Assoc. Adv. Sci.*, pp. 1–20. (See also Papers, vol. 1, pp. 157–187. Cambridge University Press, 1880), 1846.

Stokes, G. G., On the theory of oscillatory waves, *Trans. Cam. Phil. Soc.*, *8*, 441–455, 1847.

Sur, H. I., E. Özsoy, and R. Ibrayev, Chapter 16 satellite-derived flow characteristics of the Caspian Sea, in *Satellites, oceanograghy and society*, edited by D. Halpern, vol. 63 of *Elsevier Oceanography Series*, pp. 289–297, Elsevier, 2000.

Terziev, F. S., A. Kosarev, and A. A. Kerimov (Eds.), *The Seas of the USSR. Hydrometeorology and Hydrochemistry of the Seas, Vol. VI: The Caspian Sea, Issue 1: Hydrometeorological Conditions*, Gidrometeoizdat, St. Petersburg, Russia, 1992.

Trukhchev, D., A. Kosarev, D. Ivanova, and V. Tuzhilkin, Numerical analysis of the general circulation in the Caspian Sea, *Comptes Rendus de l'Academie Bulgare des Sciences, Sofia*, *48*, 35—38, 1995.

Ursell, F., Edge waves on a sloping beach, *Proc. R. Soc. London.*, *A214*, 79–97, 1952.

Vittori, G., and P. Blondeaux, Mass transport under sea waves propagating over a rippled bed, *J. Fluid Mech.*, *314*, 247–265, 1996.

Weber, J. E. H., and M. Drivdal, Radiation stress and mean drift in continental shelf waves, *Cont. Shelf Res.*, *35*, 108–116, 2012.

Weber, J. E. H., and P. Ghaffari, Mass transport in the Stokes edge wave, *J. Mar. Res.*, *67*, 213–224, 2009.

Weber, J. E. H., and P. Ghaffari, Mass transport in internal coastal Kelvin waves, *Europ. J. Mech. B/Fluids*, in press, 2014.

Weber, J. E. H., and A. Melsom, Transient ocean currents induced by wind and growing waves, *J. Phys. Oceanogr.*, *23*, 193–206, 1993.

Weber, J. E. H., and E. Støylen, Mean drift velocity in the Stokes interfacial edge wave, *J. Geophys. Res.*, *116*, C04,002, 2011.

Weber, J. E. H., G. Broström, and Ø. Saetra, Eulerian versus lagrangian approaches to the wave-induced transport in the upper ocean, *J. Phys. Oceanogr.*, *36*, 2106–2117, 2006.

Williams, R. B., and C. H. Gibson, Direct measurements of turbulence in the Pacific Equatorial Undercurrent, *J. Phys. Oceanogr.*, *4*, 104–108, 1974.

Zaker, N. H., P. Ghaffari, and S. Jamshidi, Physical study of the southern coastal waters of the Caspian Sea, off Babolsar, Mazandaran in Iran, *J . Coast. Res.*, *SI 50*, 564–569, 2007.

Zaker, N. H., P. Ghaffari, S. Jamshidi, and M. Nouranian, Currents on the southern continental shelf of the Caspian Sea off Babolsar, Mazandaran in Iran, *J. Coas. Res., SI 64*, pp. 1989–1997, 2011.

I

II

III

IV